Supporting Information: Halide Segregation in Mixed-Halide Perovskites: Influence of A-Site Cations

Alexander J. Knight, Juliane Borchert, Robert D. J. Oliver, Jay B. Patel, Paolo G. Radaelli, Henry J. Snaith, Michael B. Johnston, and Laura M. Herz*

Department of Physics, University of Oxford, Clarendon Laboratory, Parks Road, Oxford OX1 3PU, United Kingdom

E-mail: laura.herz@physics.ox.ac.uk

Contents

1 Sample Fabrication

1.1 $MAPb(Br_{0.5}I_{0.5})_3$ Thin Film Samples

$CH_3NH_3Pb(Br_{0.5}I_{0.5})_3$ thin film samples were prepared using the acetonitrile route as reported previously.[S1] In summary, the precursor salts (methylammonium iodide, MAI, GreatCell Solar; methylammonium bromide, MABr, GreatCell Solar; lead iodide, PbI_2, TCI; lead bromide, $PbBr_2$, >98%, Alfa-Aesar) were weighed stoichiometrically and dissolved in acetonitrile (Sigma Aldrich) to give a 0.5 M solution as described by Noel *et al.*[S1]

Substrates were made of z-cut quartz (area $1.3\,\mathrm{cm}^2$) were cleaned by subsequent sonication in Decon90 (1 vol% in deionised water), deionised water, acetone (Sigma Aldrich) and isopropanol (Sigma Aldrich) for 10 min each. The substrates were then dried using an N_2-gas gun before being transferred into an N_2 filled glovebox prior to deposition of the perovskite layer.

The perovskite films were fabricated using the following spincoating recipe: 70 µl of precursor solution was deposited dynamically onto the quartz substrate spinning at 2000 rpm. The films were then annealed for 30 min at 100 °C.

PMMA (poly(methyl methacrylate), Sigma Aldrich, mean molar weight $97\,000\,\mathrm{g\,mol^{-1}}$) was dissolved in chlorobenzene (Sigma Aldrich) at $150\,\mathrm{mg\,ml^{-1}}$. To form the PMMA film, 40 µl of solution was deposited dynamically onto the perovskite film at 2000 rpm, for 25 s. The films were then annealed at 100 °C for 1 min to drive off any residual solvent.

1.2 $FA_{0.83}Cs_{0.17}Pb(Br_xI_{(1-x)})_3$ Thin Film Samples

$FA_{0.83}Cs_{0.17}Pb(Br_xI_{(1-x)})_3$ thin film samples were fabricated in line with our previous report,[S2] with slight modification to account for the different substrate area and different bromide fractions. In summary, the precursors salts (formamidinium iodide, FAI, GreatCell Solar; cesium iodide, CsI, 99.99%, Alfa-Aesar; lead iodide, PbI_2, 99.999%, Alfa-Aesar; lead bromide, $PbBr_2$, >98%, Alfa-Aesar) were weighed stoichiometrically in an N_2 filled glove box. The precursor salts were dissolved in a 4:1 ratio by volume of N,N-dimethylformamide (DMF, Sigma Aldrich) to dimethyl sulfoxide (DMSO, Sigma Aldrich), to a concentration of 1.3 M. The solution was stirred overnight before deposition. To allow a conversion between perovskite emission energy and perovskite bromide content – see Section 7 – two solutions of $FA_{0.83}Cs_{0.17}PbI_3$ and $FA_{0.83}Cs_{0.17}PbBr_3$ were prepared and mixed in appropriate ratios to span the compositional range from $x = 0$ to $x = 1$. For all other photoluminescence (PL) and X-ray diffraction (XRD) measurements, the $FA_{0.83}Cs_{0.17}Pb(Br_{0.4}I_{0.6})_3$ perovskite precursor solution was prepared directly.

Substrates made of z-cut quartz (area $1.3\,\mathrm{cm}^2$) were cleaned by subsequent sonication in Decon90 (1 vol% in deionised water), deionised water, acetone (Sigma Aldrich) and isopropanol (Sigma Aldrich) for 5 min each. The substrates were then dried using an N_2 gun before being transferred into an N_2 filled glovebox prior to deposition of the perovskite layer.

The perovskite films were fabricated using the following spincoating recipe: 50 µl of precursor solution was deposited dynamically onto the quartz substrate spinning at 1000 rpm. After 5 s, the substrate accelerated at $800\,\mathrm{rpm\,s^{-1}}$, until it reached a final spin speed of 5000 rpm where it remained for 30 s. An antisolvent quench using 50 µl of Anisole (Sigma Aldrich) was performed 5 s before the end of this step. The films were then annealed at 100 °C for 30 min.

PMMA (poly(methyl methacrylate), Sigma Aldrich, mean molar weight $97\,000\,\mathrm{g\,mol^{-1}}$) was dissolved in chlorobenzene (Sigma Aldrich) at $150\,\mathrm{mg\,ml^{-1}}$. To form the PMMA film, 40 µl of solution was deposited dynamically onto the perovskite film at 2000 rpm, for 25 s. The films were then annealed at 100 °C for 1 min to drive off any residual solvent.

After deposition of the PMMA layer, the $FA_{0.83}Cs_{0.17}Pb(Br_{0.4}I_{0.6})_3$ thin film samples were annealed at 100 °C for 30 min.

2 Basic X-ray Diffraction Measurements

Figure S1 shows X-ray diffraction (XRD) patterns obtained from three $MAPb(Br_{0.5}I_{0.5})_3$ films, each spin-coated onto a quartz substrate and coated with a layer of poly(methyl methacrylate) (PMMA). Immediately following the XRD measurements shown in Figure S1, the $MAPb(Br_{0.5}I_{0.5})_3$ films were subjected to illumination for different periods of time, as part of the experiments discussed in the main text. The XRD patterns shown in Figure S1 were obtained with a Rigaku SmartLab X-ray diffractometer, and were taken from diffraction angle 10° to 50° 2θ, at a scan speed of $0.02\,^\circ\,s^{-1}$. The Cu-$K_{\alpha 1}$ line was used as incident radiation, and in order to correct against sample tilt, a relevant z-cut quartz peak in the data was used as a reference and fixed to $2\theta = 16.43°$.

Figure S2 shows an XRD pattern obtained from an $FA_{0.83}Cs_{0.17}Pb(Br_{0.4}I_{0.6})_3$ perovskite film, spin-coated onto a quartz substrate and coated with a layer of poly(methyl methacrylate) (PMMA). Immediately following the XRD measurement shown in Figure S2, the $FA_{0.83}Cs_{0.17}Pb(Br_{0.4}I_{0.6})_3$ film was subjected to 6 h of illumination as part of the experiments discussed in the main text. The XRD pattern in Figure S2 was obtained with a PANalytical X'Pert Powder X-Ray Diffractometer, and was taken from diffraction angle 10° to 50° 2θ, at a scan speed of $0.01\,^\circ\,s^{-1}$. The Cu-$K_{\alpha 1}$ line was used as incident radiation, and in order to correct against sample tilt, the z-cut quartz peak in the data was used as a reference and fixed to $2\theta = 16.43°$.

Both the $MAPb(Br_{0.5}I_{0.5})_3$ and the $FA_{0.83}Cs_{0.17}Pb(Br_{0.4}I_{0.6})_3$ perovskite were assigned a cubic unit cell in the space group $Pm\bar{3}m$. Texturing effects had a clear influence on the amplitude of the XRD peaks across the two perovskite compositions, which is especially clear in Figure S1 by the dominance of the (100) and (200) peaks for the $MAPb(Br_{0.5}I_{0.5})_3$ perovskite.

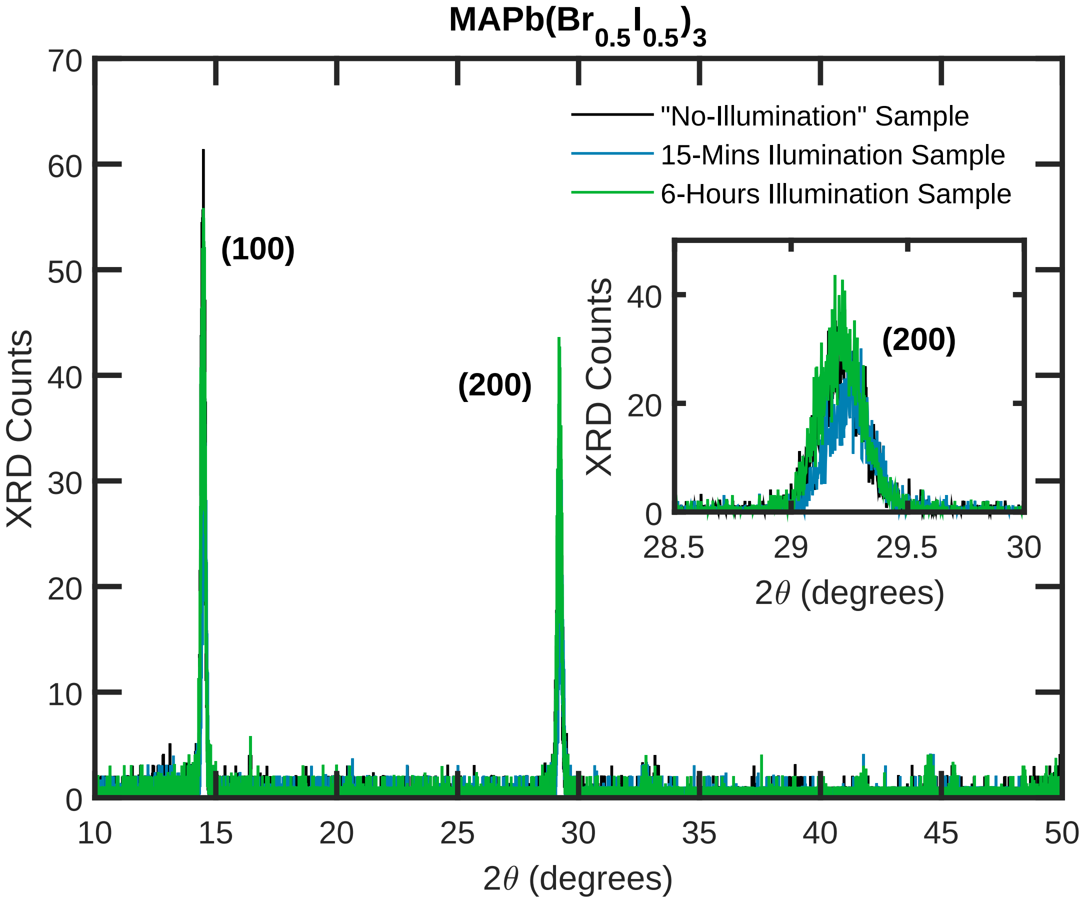

Figure S1: XRD patterns taken from three separate MAPb(Br$_{0.5}$I$_{0.5}$)$_3$ thin films coated with PMMA, with the XRD measurements made prior to any illumination having occurred. The Cu-K$_{\alpha1}$ line was used as incident radiation. After these XRD measurements, the three films were then used in the no-illumination, 15-minute, and 6-hour illumination experiments discussed in the main text. The inset shows a zoomed region of the graph highlighting the pseudo-cubic (200) peak of the perovskite XRD pattern, which is the peak used for the analysis discussed in the main text.

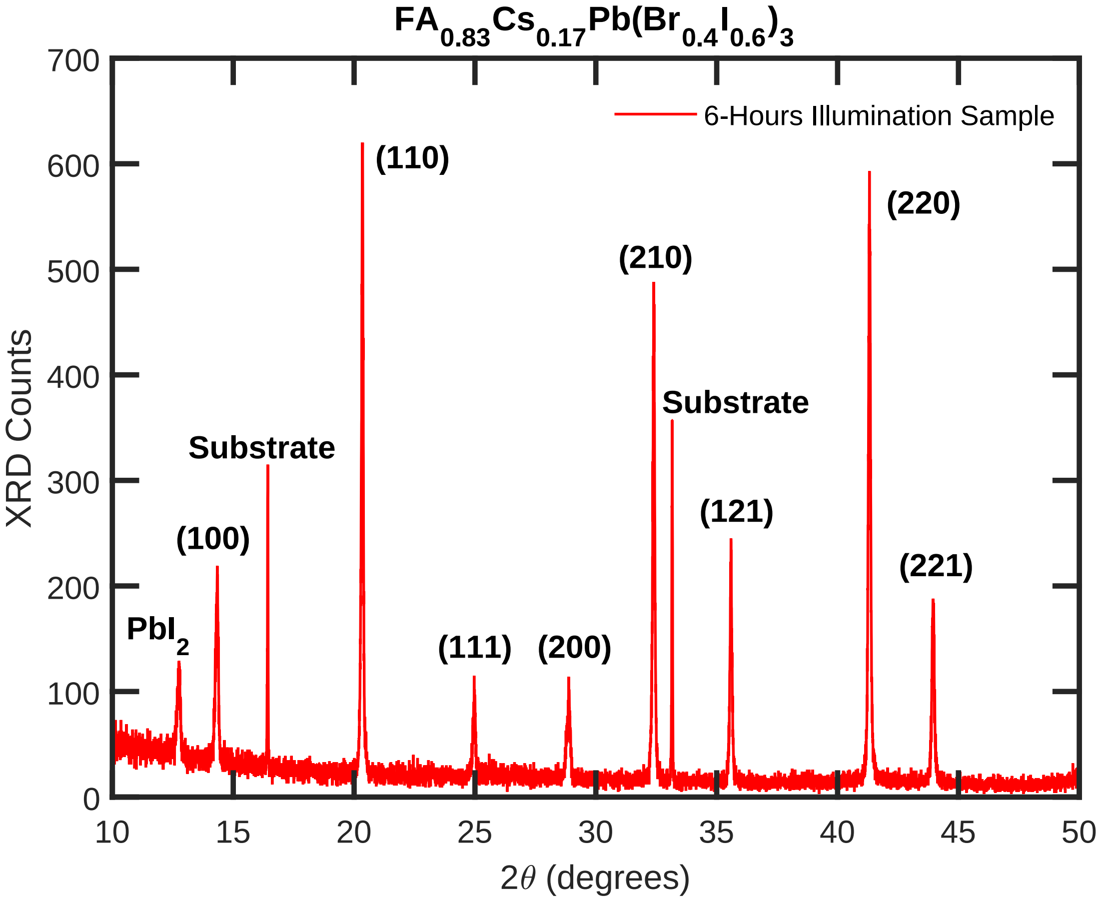

Figure S2: XRD pattern taken from an $FA_{0.83}Cs_{0.17}Pb(Br_{0.4}I_{0.6})_3$ thin film coated with PMMA, with the XRD measurements made prior to any illumination having occurred. The Cu-$K_{\alpha 1}$ line was used as incident radiation. After this XRD measurement, the perovskite film was then used in the 6-hour illumination experiment discussed in the main text. The pseudo-cubic (220) peak of the perovskite pattern is labelled, which is the peak used for the analysis discussed in the main text.

2.1 Peak Width Analysis

In order to gain a simple estimate of the crystallinity of the $\mathrm{MAPb(Br_{0.5}I_{0.5})_3}$ and the $\mathrm{FA_{0.83}Cs_{0.17}Pb(Br_{0.4}I_{0.6})_3}$ perovskite thin films, Table S1 presents the full width at half-maximum (FWHM) of the XRD peaks shown in Figures S1 and S2.

Table S1: Full width at half-maximum (FWHM) values of XRD peaks recorded from three different $\mathrm{MAPb(Br_{0.5}I_{0.5})_3}$ perovskite thin films (XRD data shown in Figure S1), and an $\mathrm{FA_{0.83}Cs_{0.17}Pb(Br_{0.4}I_{0.6})_3}$ thin film (XRD data shown in Figure S2). The FWHM data from the XRD pattern of the $\mathrm{FA_{0.83}Cs_{0.17}Pb(Br_{0.4}I_{0.6})_3}$ thin film were extracted directly from the data. The XRD patterns of the three $\mathrm{MAPb(Br_{0.5}I_{0.5})_3}$ thin films display a significant amount of noise, and so the corresponding peak FWHM values were extracted from Gaussian fits to the data.

Sample	Peak	FWHM (° 2θ)
$\mathrm{MAPb(Br_{0.5}I_{0.5})_3}$, (Sample Subsequently Used in "No Illumination" Experiment)	(100)	0.21
	(200)	0.23
$\mathrm{MAPb(Br_{0.5}I_{0.5})_3}$, (Sample Subsequently Used in "15-Mins Illumination" Experiment)	(100)	0.21
	(200)	0.23
$\mathrm{MAPb(Br_{0.5}I_{0.5})_3}$, (Sample Subsequently Used in "6-Hours Illumination" Experiment)	(100)	0.20
	(200)	0.23
$\mathrm{FA_{0.83}Cs_{0.17}Pb(Br_{0.4}I_{0.6})_3}$, (Sample Subsequently Used in "6-Hours Illumination" Experiment)	(100)	0.14
	(110)	0.09
	(111)	0.10
	(200)	0.13
	(210)	0.09
	(121)	0.08
	(220)	0.10
	(221)	0.13

From the data shown in Table S1, it is clear the three $\mathrm{MAPb(Br_{0.5}I_{0.5})_3}$ thin films possess an extremely similar level of crystallinity, as the FWHM values for their respective peaks are nearly identical across the three films. Furthermore, the FWHM values recorded from the $\mathrm{FA_{0.83}Cs_{0.17}Pb(Br_{0.4}I_{0.6})_3}$ thin film are shown to be consistently slightly smaller than the peaks recorded from the $\mathrm{MAPb(Br_{0.5}I_{0.5})_3}$ films. The difference in peak widths between the $\mathrm{MAPb(Br_{0.5}I_{0.5})_3}$ and $\mathrm{FA_{0.83}Cs_{0.17}Pb(Br_{0.4}I_{0.6})_3}$ films suggests that the crystallinity between the films is similar, but that the $\mathrm{FA_{0.83}Cs_{0.17}Pb(Br_{0.4}I_{0.6})_3}$ film likely possesses slightly superior crystallinity, corroborating the known result in the literature that the A-site composition of a perovskite has a significant impact on the crystallinity of the resulting film.[S3–S5] As we discuss in the main text, the dependence of the film crystallinity on the A-site cation composition could partly explain the strong dependence of phase-stability on the A-site cation composition of the material.

3 Differences in Perovskite Thin Films

Other than the composition of the A-site cations, various small differences between the examined $MAPb(Br_{0.5}I_{0.5})_3$ and $FA_{0.83}Cs_{0.17}Pb(Br_{0.4}I_{0.6})_3$ films may have had slight effects on the resulting halide segregation dynamics.

Halide Content:

The halide composition of a perovskite material can have a large impact on the resulting halide segregation dynamics, especially if the perovskite material is very close to a stable-unstable compositional boundary. In our case, we note that the halide compositions of the $MAPb(Br_{0.5}I_{0.5})_3$ and $FA_{0.83}Cs_{0.17}Pb(Br_{0.4}I_{0.6})_3$ materials are very similar, and close to a 50:50 iodide:bromide ratio, which is often observed to be the least stable halide content region.[S6] Furthermore, around this 50:50 halide region it is typically observed in the literature that perovskite thin films exhibit similar halide segregation dynamics. Hence, we do not expect there to be much difference in the segregation dynamics of an $MAPb(Br_{0.5}I_{0.5})_3$ and an $MAPb(Br_{0.4}I_{0.6})_3$ thin film. The influence of the halide composition is much more apparent when the perovskite is at the boundary of stability conditions,[S7] however in our case the halide content was, for both the MA-based and FA/Cs-based perovskite compositions, well within the expected unstable compositional range,[S6] and the illumination intensity used was significantly in excess of that typically required to induce halide segregation.[S6] Hence based on what is known from previous literature studies, it is not expected that the slight difference in the halide content of our two examined materials would be a decisive factor in the phase-segregation dynamics, and we conclude that the predominant factor on the stability of the two perovskite compositions was the stoichiometry of the A-site cations.

Manufacturing Route:

The different solvents and manufacturing routes used to create the $MAPb(Br_{0.5}I_{0.5})_3$ and $FA_{0.83}Cs_{0.17}Pb(Br_{0.4}I_{0.6})_3$ thin films (see Section 1) likely had an effect on the formation mechanisms of the two different perovskite films, and as a result on the subsequent halide segregation dynamics. The different precursor solvents were selected, however, in order to manufacture high-quality, homogeneous perovskite films that would not be subjected to any anomalous ionic behaviour. In previous studies we have found that utilizing acetonitrile leads to both better-quality $\mathrm{MAPbI_3}$[S1] and $\mathrm{MAPbBr_3}$[S8] perovskite thin films than manufacturing routes involving DMF, and in this study a similar acetonitrile route was elected for use in manufacturing our $\mathrm{MAPb(Br_{0.5}I_{0.5})_3}$ films. FA and Cs do not dissolve in acetonitrile, and so a different manufacturing route involving DMF and DMSO was used for the $\mathrm{FA_{0.83}Cs_{0.17}Pb(Br_{0.4}I_{0.6})_3}$ films, a route which we have also previously optimised.[S2]

Results in the literature suggest that FA/Cs-based perovskites have a significantly higher crystallinity and photo-stability against halide segregation when compared against MA-based perovskite films, regardless of the manufacturing methods used (assuming all films are of a high quality, which is the case in this study, given that the routes were separately optimized, as discussed above),[S6] and high-quality perovskite films of the same composition are often observed to possess similar stability properties.[S6] Therefore, while the two different manufacturing methods used in our study could have resulted in some differences in the photo-stability of the two otherwise identical perovskite compositions, we believe in this case the composition of the A-site cation had a more dominant effect on the segregation dynamics than the manufacturing route. In our study we purposely compared two high-quality materials that are known to have extremely different stability properties against halide segregation because of their A-cation composition,[S6] and we therefore conclude that the composition of our samples was the dominant factor on the underlying halide ion dynamics.

Crystallinity:

The quality and crystallinity of the $\mathrm{MAPb(Br_{0.5}I_{0.5})_3}$ and $\mathrm{FA_{0.83}Cs_{0.17}Pb(Br_{0.4}I_{0.6})_3}$ perovskite thin films were almost certainly different due to the differences in the A-site cation compositions and the resulting formation dynamics of the films, and this likely affected the halide segregation dynamics of the films. Given the data in the literature, we expect that the composition of the precursor solutions dictates, to a significant extent, the crystallinity of the resulting perovskite films, which is partly an explanation of why perovskites with certain

A-site cations are more stable to halide segregation than others.[S6] We argue that the A-site composition of the perovskite and its resulting crystallinity are not separable effects, and that in the consideration of why FA/Cs-based perovskites are more stable to halide segregation than MA-based perovskites, the generally superior crystallinity of the FA/Cs-based perovskites that results from their A-site cation makeup must be taken into consideration. In the main text we conclude that grain boundaries in our $MAPb(Br_{0.5}I_{0.5})_3$ films are a critical influence on the halide segregation mechanism, and the lack of these grain boundaries in $FA_{0.83}Cs_{0.17}Pb(Br_{0.4}I_{0.6})_3$ films goes some way to explaining their superior photo-stability, highlighting the links between A-site cation composition, crystallinity, and phase-stability.

PbI_2 Content:

The PbI_2 content of the $MAPb(Br_{0.5}I_{0.5})_3$ and $FA_{0.83}Cs_{0.17}Pb(Br_{0.4}I_{0.6})_3$ films may have been different, as highlighted in Figure S12 and Figure S13 below. The role of PbI_2 on the halide segregation dynamics in mixed-halide perovskite materials has not been well-explored, however we believe the effect of small amounts of PbI_2 on these dynamics would be relatively benign. Recent work has shown that the boundary between perovskite material and PbI_2 inclusions is actually remarkably clean, and would therefore not be expected to introduce crystallinity defects, charge-carrier trap states, or other factors that could potentially affect the halide segregation dynamics in these materials.[S9] Additionally, the bandgap of PbI_2 is generally higher than that of the surrounding perovskite, meaning that charge carriers would not be expected to enter or interact with these regions in a perovskite structure,[S10] making the inclusion of PbI_2 in our films largely benign with regards to the halide segregation dynamics.

4 Additional XRD Analysis of $FA_{0.83}Cs_{0.17}Pb(Br_{0.4}I_{0.6})_3$

Figure S3a presents XRD data taken from an $FA_{0.83}Cs_{0.17}Pb(Br_{0.4}I_{0.6})_3$ perovskite film, coated with PMMA, over the course of 6 h of illumination under $190\,\mathrm{mW\,cm^{-2}}$ intensity, 470 nm wavelength light. The peak shown in these data is the (220) diffraction peak of the perovskite structure, as recorded using our in-situ setup described in Section 5.1. These XRD data have not been background corrected, and are plotted on a logarithmic y-axis in order to emphasize the growth of signal in the high-angle tail of the (220) peak, the origin of which is discussed below in Section 4.1.

Figure S3b shows the mean value (red) and maximum amplitude (blue) positions of the background-corrected XRD diffraction amplitude in S3a. While the angle corresponding to the (220) XRD peak is shown by the blue plot in Figure S3b to have shifted to lower 2θ values over the 6 h of illumination, this effect is counter-balanced by the growth of signal in the high-angle tail of the (220) XRD peak (highlighted by the arrow in Figure S3a). Therefore, as shown by the red plot in Figure S3b, there is minimal overall shift in the mean value of the angle distribution of the XRD diffraction amplitudes.

The minor shift from 41.32° to 41.25° 2θ of the mean value of the XRD angle as highlighted by the red plot in Figure S3b could be the result of several factors. Firstly, strain in the perovskite crystal can alter the spacing between lattice planes, resulting in a change in angular position of XRD diffraction peaks. The introduction of lattice strain throughout the perovskite material could therefore alter the mean position of the recorded XRD signal. Secondly, the X-ray reflectivity of iodide-rich and bromide-rich perovskite regions are not equivalent, with XRD measurements usually being more sensitive to more electron-rich ions.[S11] As a result, it is possible for the simple rearrangement of iodide and bromide ions within the $FA_{0.83}Cs_{0.17}Pb(Br_{0.4}I_{0.6})_3$ thin film to have moved the mean position of the XRD signal towards lower 2θ angles, simply by virtue of the higher X-ray reflectivity expected of the iodide-rich perovskite regions. Thirdly, crystallinity effects could emphasize the XRD signal of some regions of perovskite material over others, allowing the center position of the

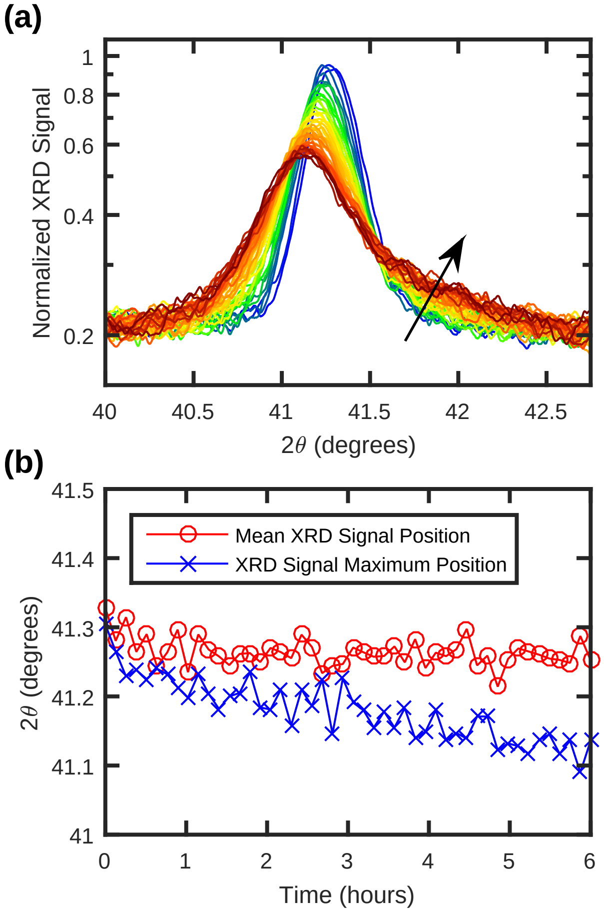

Figure S3: (a) Smoothed, normalized XRD patterns displaying the (220) diffraction peak of a PMMA-coated $FA_{0.83}Cs_{0.17}Pb(Br_{0.4}I_{0.6})_3$ perovskite film under $190\,mW\,cm^{-2}$ intensity illumination over the course of 6 h. The data are plotted on a logarithmic y-axis and are not background corrected in order to emphasize the growth of signal in the high-angle peak tail ($\sim$41.5°–42.75° 2θ). The Cu-$K_{\alpha 1}$ line was used as incident radiation. (b) The mean position (red) and the position of the maximum signal (blue) of the background-corrected XRD data corresponding to the plots in (a) over time.

XRD peak to shift. Finally, while we conclude in the main text that there was no significant degradation of the perovskite material into non-perovskite structures over the course of the conducted experiments, minor losses of perovskite structure could have contributed to the minor shift of overall XRD signal.

4.1 Origin of High-Angle XRD Signal

The increase of high-angle signal in the XRD pattern of the $FA_{0.83}Cs_{0.17}Pb(Br_{0.4}I_{0.6})_3$ perovskite thin film – shown in Figure S3a – indicates the formation of a perovskite phase with a closer lattice-spacing than that of the original, bulk $FA_{0.83}Cs_{0.17}Pb(Br_{0.4}I_{0.6})_3$ phase. Given the ionic radii of the constituent elements of the $FA_{0.83}Cs_{0.17}Pb(Br_{0.4}I_{0.6})_3$ perovskite, the emerging phase must be bromide-rich, cesium-rich, or enriched in both bromide and cesium. The range of 2θ over which the XRD signal is observed to increase (∼41.5°–42.75°) corresponds to a cubic-phase perovskite material with a range of lattice parameters between 5.98–6.15 Å. Considering single-cation perovskites, this range of lattice parameters approximately corresponds to perovskite materials such as $FAPb(Br_xI_{(1-x)})_3$ for $0.5 \leq x \leq 1.0$[S12,S13] and $CsPb(Br_xI_{(1-x)})_3$ for $0 \leq x \leq 0.4$.[S14] Therefore, the range of perovskite compositions that could generate the 2θ signal observed at the highest angles – ∼42.75° – runs from $FAPbBr_3$ to $CsPb(Br_{0.4}I_{0.6})_3$. The bandgap values reported in the literature for both $FAPbBr_3$ and $CsPb(Br_{0.4}I_{0.6})_3$ perovskites – approximately 2.3 eV[S12,S13] and 1.9 eV,[S14] respectively – are larger than that of the bulk $FA_{0.83}Cs_{0.17}Pb(Br_{0.4}I_{0.6})_3$ perovskite material used in this study, which has an initial PL peak position of ∼1.76 eV, as shown in Figure 1b of the main text. Therefore the formation of either a higher-bandgap $FAPbBr_3$-rich phase or a higher-bandgap $CsPb(Br_{0.4}I_{0.6})_3$-rich phase – or, in principle, a phase enriched with a blend of these compositions – would likely red-shift the bandgap of the remaining bulk perovskite phase. The PL signal associated with the bulk $FA_{0.83}Cs_{0.17}Pb(Br_{0.4}I_{0.6})_3$ perovskite phase did in fact red-shift over the course of the experiment, see Figure 4a and the surrounding discussion in the main text, consistent with the emergence of any of the aforementioned higher-bandgap phases.

In principle, according to the discussion above, the emerging XRD signal observed at ∼42.75° 2θ in Figure S3a could be a $0.83 : 0.17$ blend of $FAPbBr_3$ and $CsPb(Br_{0.4}I_{0.6})_3$ perovskites – a phase composition of around $FA_{0.83}Cs_{0.17}Pb(Br_{0.9}I_{0.1})_3$. The formation of an $FA_{0.83}Cs_{0.17}Pb(Br_{0.9}I_{0.1})_3$ phase from the $FA_{0.83}Cs_{0.17}Pb(Br_{0.4}I_{0.6})_3$ bulk would require no A-site cation movement, only halide movement, and represents a strong contender for the XRD signal observed at ∼42.75° 2θ. However there are reasons to doubt $FA_{0.83}Cs_{0.17}Pb(Br_{0.9}I_{0.1})_3$ as a candidate for the emerging XRD signal shown in Figure S3a. Due to the preferential binding of lead to bromide as compared to iodide,[S15,S16] it would be unexpected – but would in principle match our observations – for the bromide ions in the bulk perovskite material to separate out – forming the high-angle XRD tail – and leave the bulk perovskite enriched in iodide – which would consequently shift to lower 2θ angles. Due to the different strengths of the lead-halide bonds, it would instead be considered more likely for the iodide ions to separate out, leaving a bromide-enriched bulk phase – which has been observed previously[S17] – or for both the iodide and bromide ions to separate out from the bulk phase – which we observed for the $MAPb(Br_{0.5}I_{0.5})_3$ thin film, see the discussion surrounding Figure 1c of the main text. As a result, we propose that the more likely explanation for the growth the high-angle XRD tail shown in Figure S3a involves the movement of A-site cations – a similar conclusion to that reached in the work of Lin *et al.* on related perovskite materials[S2] – although we acknowledge the possibility of a mechanism based purely on halide ion movement.

Given the likelihood that there is some A-site cation movement involved in the formation of the high-angle tail of the XRD signal in Figure S3a, we can conclude that the composition of the remaining bulk perovskite phase must become enriched in either FA or cesium. As shown by Rehman *et al.*, the stability of $FA_{(1-y)}Cs_yPb(Br_xI_{(1-x)})_3$ perovskite systems against halide segregation is extremely sensitive to the cesium content of the composition, y, with maximum stability observed for $y \sim 0.2$.[S3] We therefore propose that any change – be it FA- or Cs-enrichment – in the A-site composition of our bulk $FA_{0.83}Cs_{0.17}Pb(Br_{0.4}I_{0.6})_3$ perovskite would greatly decrease the overall stability of the perovskite film against halide segregation, as Rehman *et al.* have shown that even slightly away from the $y \sim 0.2$ composition halide segregation occurs over the course of minutes, rather than hours.[S3] Additionally, halide segregation is known to rapidly proceed in purely Cs-based[S14] and FA-based perovskites.[S17,S18] We therefore propose that the rate of halide segregation within the bulk phase of the $FA_{0.83}Cs_{0.17}Pb(Br_{0.4}I_{0.6})_3$ perovskite is intimately tied to – and indeed likely rate-limited by – the amount of A-site cation movement within the film in a suggested 2-step mechanism. In the first step of this proposed mechanism, incident illumination causes a movement of A-site cations in the perovskite film, resulting in the formation of a minority phase enriched in either FA or cesium, and results in the corresponding enrichment of the bulk phase in either cesium or FA, respectively. As the second step, the bulk – now slightly displaced from the maximally stable composition of $y \sim 0.2$ – experiences a degree of halide segregation as a result of the illumination. Under this proposed mechanism the amount of halide segregation the $FA_{0.83}Cs_{0.17}Pb(Br_{0.4}I_{0.6})_3$ perovskite experiences would be expected to be linked with the amount of A-site cation movement that occurs under illumination, and the resulting bulk enrichment in either cesium or FA. The link between A-site cation movement and halide segregation is corroborated by Figure S4, which shows that the ratio of the low-energy, iodide-rich phase PL signal to the initial, mixed-phase PL signal (blue plot, which increases as the amount of halide segregation builds up in the perovskite film) is correlated with the integral of the high angle XRD tail shown in Figure S3a (orange plot, which increases with increasing amount of A-site cation movement and separation).

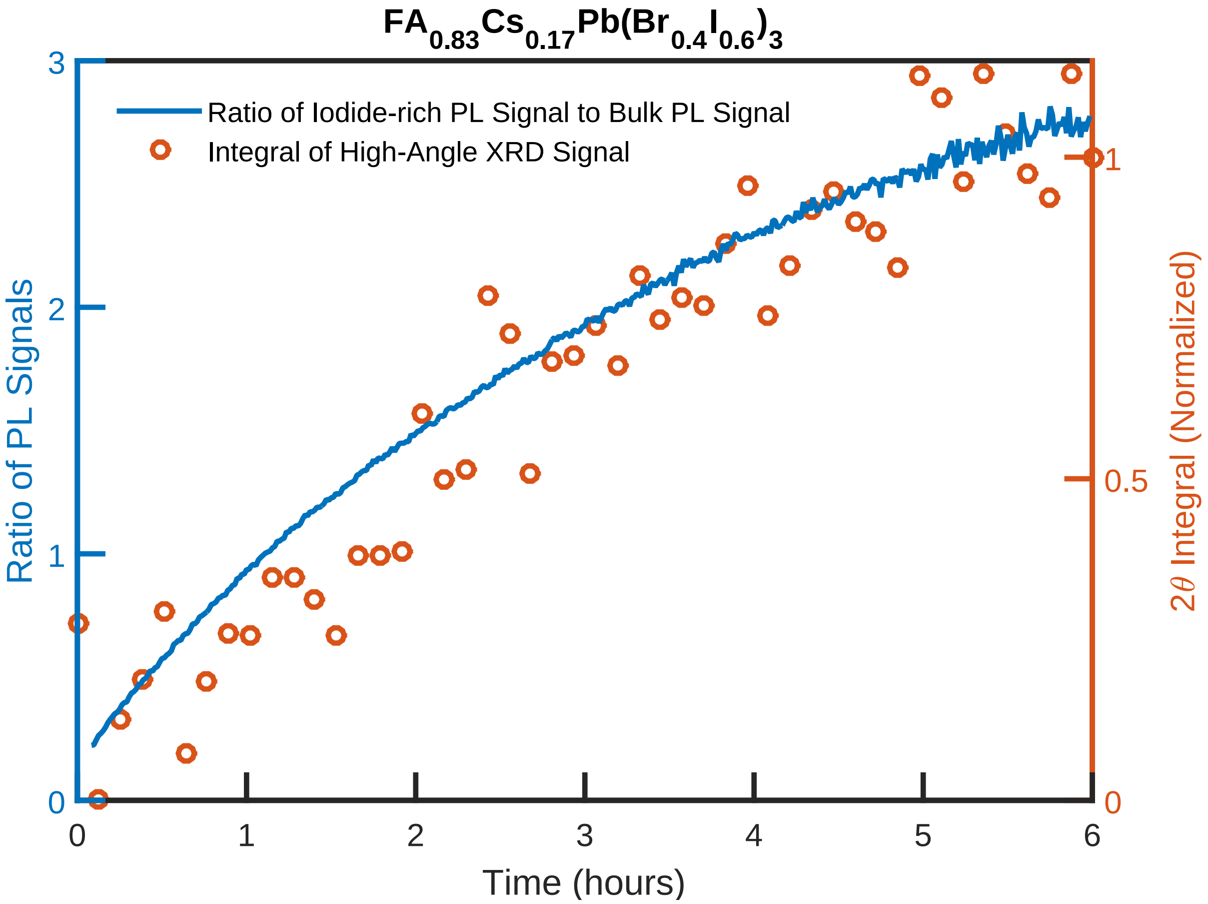

Figure S4: Correlation between the amount of halide segregation and amount of A-site cation movement observed in a PMMA-coated $FA_{0.83}Cs_{0.17}Pb(Br_{0.4}I_{0.6})_3$ perovskite film under 190 mW cm^{-2} intensity illumination over the course of 6 h. The blue plot shows the ratio of the low-energy, iodide-rich PL signal to the initial, mixed-phase PL signal, which increases as halide segregation progresses in the perovskite film (during halide segregation the iodide-rich PL signal increases and the mixed-phase PL signal decreases, and so the ratio of the two necessarily increases). The missing blue data points near the origin indicate the region where it is difficult to resolve two distinct peaks in the PL spectrum. The orange plot shows the integral of the high-angle tail of the (220) peak from the XRD pattern of the same $FA_{0.83}Cs_{0.17}Pb(Br_{0.4}I_{0.6})_3$ thin film – see Figure S3a. The integral was taken from 41.5° to 42.75° 2θ and was set to zero and normalized near the start and end, respectively, of the 6 h illumination period for clarity.

5 Concurrent, in-situ XRD and PL Measurements

5.1 Measurement Overview

Other than the data presented in Figure S1, S2, S10, S12, S13 and S14, the data presented in the main article and in this SI were taken utilizing a home-built insert to an X-ray diffractometer, allowing us to take concurrent, in-situ, PL and XRD measurements while illuminating the investigated sample. The experimental setup consisted of a small setup of optical equipment integrated within a Rigaku SmartLab X-ray diffractometer. The illumination source used for the PL measurements was an LDH-D-C-470 fibre-coupled laser, with an emission wavelength of ∼470 nm. Optical fibres were used to feed the incident illumination from the laser source into the Rigaku SmartLab diffractometer, whereupon the laser light was launched into free space and onto the sample. A lens was used to control the laser beam illumination area and intensity. The PL emitted from the sample was collected and coupled into another optical fibre, before being led out of the Rigaku SmartLab and into an Ocean Optics USB2000 spectrometer.

The XRD measurements were taken via the Rigaku SmartLab diffractometer that contained the optical insert, with a HyPix-3000 2D X-ray detector, utilizing a Bragg-Brentano reflection geometry. The Cu-$K_{\alpha1}$ line was used as incident radiation. The 2-dimensional detection face of the X-ray detector allowed us to measure over a range of 2θ values without moving the X-ray source, the sample, or the detector. Utilizing this static experimental setup for XRD measurements, we were able to take these at a sufficiently fast rate to gain time-resolved information about the halide segregation process. We note that, because of the flat measurement face of the X-ray detector, only a small area of the detector face would have been in a true Bragg-Brentano geometry over the course of the conducted experiments. However, given the large distance between the detector and the sample (∼0.3 m) as compared to the dimensions of the detector face (∼0.05 m) we do not expect the geometry of the setup to have had a significant effect on the measurement results.

The XRD measurements were taken over ranges of 2θ that correspond to particularly prominent XRD peaks in the XRD patterns of the two perovskite materials – the (200) and the (220) peak for the $\mathrm{MAPb(Br_{0.5}I_{0.5})_3}$ and $\mathrm{FA_{0.83}Cs_{0.17}Pb(Br_{0.4}I_{0.6})_3}$ perovskites, respectively (see Figure S1 and S2 for full XRD patterns of the $\mathrm{MAPb(Br_{0.5}I_{0.5})_3}$ and $\mathrm{FA_{0.83}Cs_{0.17}Pb(Br_{0.4}I_{0.6})_3}$ thin film samples, respectively). The amplitude of the XRD peaks varied across the two perovskite compositions due to texturing effects, and so different peaks were selected for the two compositions. Second-order peaks – the (200) and (220) peaks as opposed to the (100) and (110) peaks – were selected for examination in order to provide a good 2θ resolution.

5.2 XRD Peak Amplitude Behavior

Figure S5 plots the time-resolved amplitude of the (200) peak from the XRD patterns of several $\mathrm{MAPb(Br_{0.5}I_{0.5})_3}$ thin films, and the (220) peak from the XRD pattern of an $\mathrm{FA_{0.83}Cs_{0.17}Pb(Br_{0.4}I_{0.6})_3}$ thin film. Figure S5a shows the behavior of the XRD peaks when the perovskite films are subjected to $190\,\mathrm{mW\,cm^{-2}}$ intensity, 470 nm wavelength illumination, and Figure S5b shows the behavior of the same peaks following the corresponding periods, but when the perovskite films were left in darkness. The amplitudes of the XRD peaks in both Figure S5a and S5b are normalized to the initial value the XRD peak had before any period of illumination or darkness had commenced. The axes in Figure S5b are shifted so that the data plots begin at the origin, to allow for easier comparison of the data.

Figure S5a shows that the (200) XRD peak of the $\mathrm{MAPb(Br_{0.5}I_{0.5})_3}$ perovskite films, under illumination, decreased in amplitude faster than the (220) XRD peak of the $\mathrm{FA_{0.83}Cs_{0.17}Pb(Br_{0.4}I_{0.6})_3}$ thin film. The data in Figure S5a therefore shows that the $\mathrm{MAPb(Br_{0.5}I_{0.5})_3}$ perovskite experienced faster ionic re-arrangement when exposed to illumination, as compared to the $\mathrm{FA_{0.83}Cs_{0.17}Pb(Br_{0.4}I_{0.6})_3}$ perovskite. Similarly, Figure S5b shows that the (200) XRD peak of the $\mathrm{MAPb(Br_{0.5}I_{0.5})_3}$ perovskite films increased in amplitude faster than the (220) XRD peak of the $\mathrm{FA_{0.83}Cs_{0.17}Pb(Br_{0.4}I_{0.6})_3}$ thin film when the

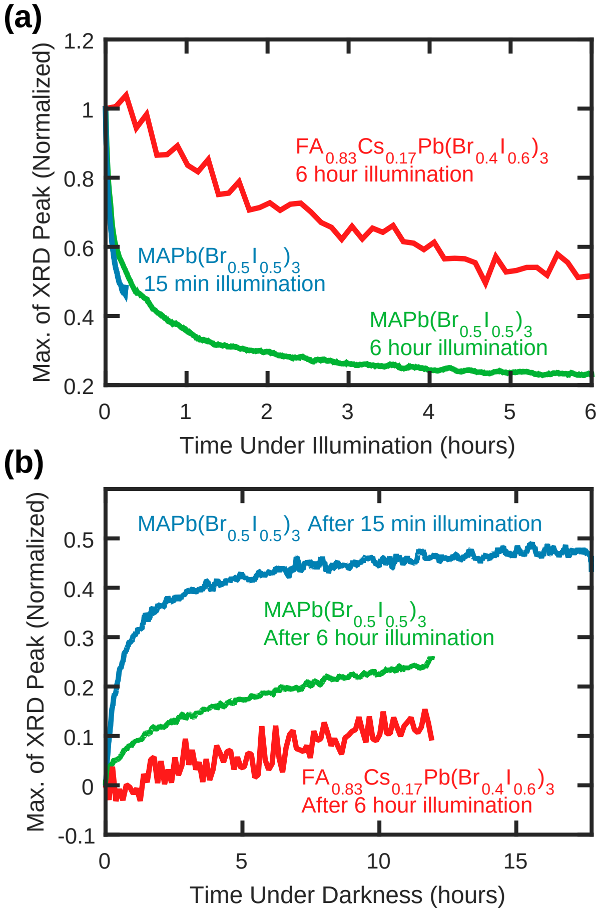

Figure S5: The maximum amplitude of the (200) peak (MAPb($Br_{0.5}I_{0.5}$)$_3$) and the (220) peak ($FA_{0.83}Cs_{0.17}Pb(Br_{0.4}I_{0.6})_3$) in the XRD pattern of metal halide perovskite films coated with PMMA. (a) The behavior of the XRD peak amplitudes during perovskite film illumination under either 15 min or 6 h of 190 mW cm^{-2} intensity light of 470 nm wavelength. The XRD peak amplitudes are normalized to their initial values before any illumination. (b) The behavior of the XRD peak amplitudes under darkness, immediately after the corresponding period of perovskite film illumination. The XRD peak amplitudes are normalized to the initial value the XRD peak had before any period of illumination or darkness had commenced, and the axes are shifted so that the plots begin at the origin to allow for an easier comparison of the data.

perovskites were left in darkness after the corresponding periods of illumination. Figure S5b therefore suggests that the $MAPb(Br_{0.5}I_{0.5})_3$ perovskite also experienced faster ionic movement under darkness than the $FA_{0.83}Cs_{0.17}Pb(Br_{0.4}I_{0.6})_3$ perovskite. Figure S5b also shows that the XRD peak of the $MAPb(Br_{0.5}I_{0.5})_3$ perovskite film exposed to only 15 min of illumination recovered in amplitude under darkness faster than the peak of the similar perovskite film exposed to 6 h of illumination, suggesting that the longer illumination period induced more severe changes in the perovskite material. A comparison between Figure S5a and S5b reveals that the amplitude of the XRD peaks experienced faster dynamics under illumination than under darkness, for both the $\mathrm{MAPb(Br_{0.5}I_{0.5})_3}$ and $\mathrm{FA_{0.83}Cs_{0.17}Pb(Br_{0.4}I_{0.6})_3}$ perovskite compositions.

5.3 PL and XRD Before and After Illumination and Darkness

Figure S6 presents PL spectra and XRD patterns recorded from an $\mathrm{MAPb(Br_{0.5}I_{0.5})_3}$ perovskite thin film, before and after 15 min of $190\,\mathrm{mW\,cm^{-2}}$ intensity illumination, and after a subsequent period of darkness. Figure S7 shows PL spectra and XRD patterns recorded for an $\mathrm{MAPb(Br_{0.5}I_{0.5})_3}$ perovskite thin film, before and after 6 h of $190\,\mathrm{mW\,cm^{-2}}$ intensity illumination, and after a subsequent period of darkness. Figure S8 presents XRD patterns recorded for an $\mathrm{MAPb(Br_{0.5}I_{0.5})_3}$ thin film at the start and end of 18 h of darkness, with XRD measurements made of the film throughout the 18 h period. Figure S9 presents PL spectra and XRD patterns recorded from an $\mathrm{FA_{0.83}Cs_{0.17}Pb(Br_{0.4}I_{0.6})_3}$ perovskite thin film sample, before and after 6 h of $190\,\mathrm{mW\,cm^{-2}}$ intensity illumination, and after subsequent periods of darkness. For the XRD measurements in Figure S6b, S7b, S8, and S9b the Cu-$\mathrm{K}_{\alpha 1}$ line was used as incident radiation.

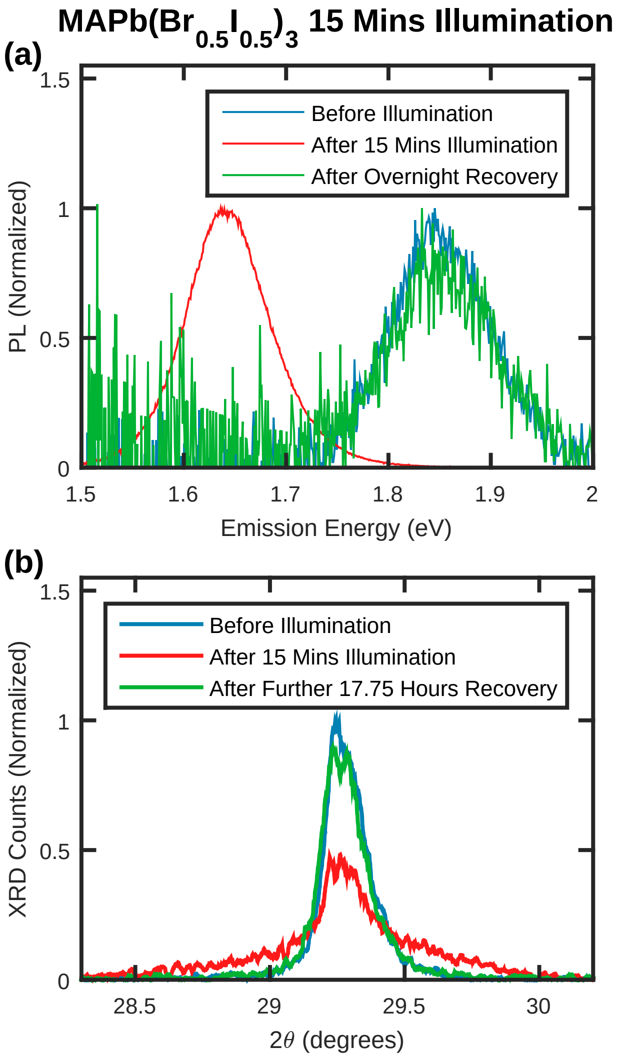

Figure S6: (a) PL spectra of an $\mathrm{MAPb(Br_{0.5}I_{0.5})_3}$ thin film coated with PMMA, recorded before and after 15 min of 190 mW cm^{-2}, 470 nm wavelength illumination, and after a period of overnight recovery (around 24 h). (b) XRD patterns of the same film, recorded in-situ before and after the same 15 min of 190 mW cm^{-2} illumination, and after a period of 17 h, 45 min of darkness subsequent to the 15 min of illumination. "Before Illumination" (blue) data measurements in (a) and (b) were recorded at approximately the same time, as were the "After 15 Mins Illumination" (red) data measurements. XRD measurements were continuously taken of the film throughout the 15 min of illumination and the further 17 h and 45 min of darkness.

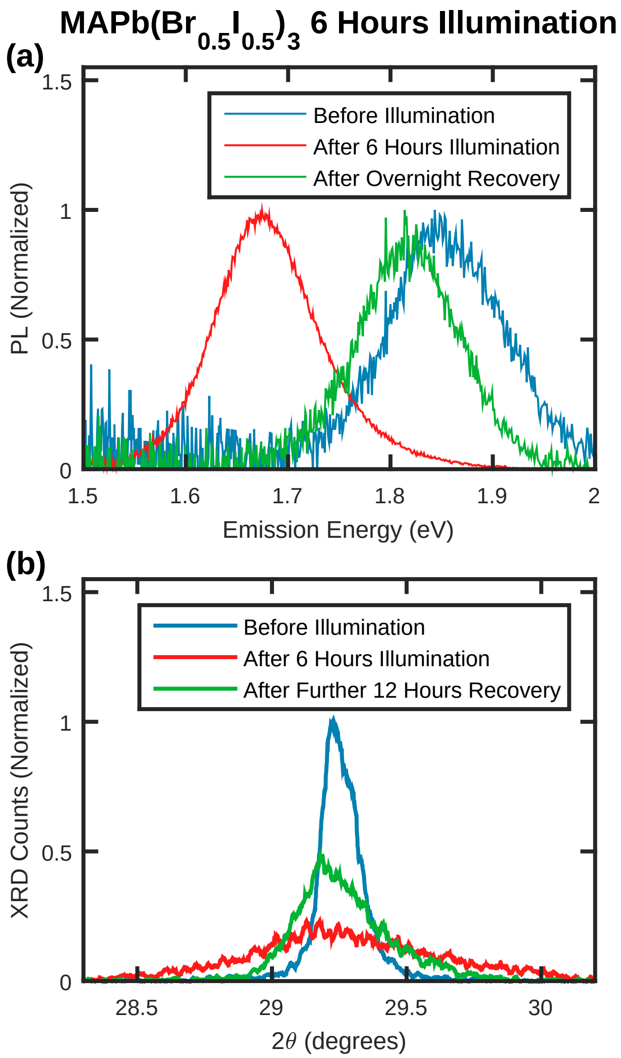

Figure S7: (a) PL spectra of an $\mathrm{MAPb(Br_{0.5}I_{0.5})_3}$ thin film coated with PMMA, recorded before and after 6 h of $190\,\mathrm{mW\,cm^{-2}}$, 470 nm wavelength illumination, and after a period of overnight recovery (around 18 h). (b) XRD patterns of the same film, recorded in-situ before and after the 6 h of $190\,\mathrm{mW\,cm^{-2}}$ illumination, and after a period of 12 h of darkness subsequent to the 6 h of illumination. "Before Illumination" (blue) data measurements in (a) and (b) were recorded at approximately the same time, as were the "After 6 Hours Illumination" (red) data measurements. XRD measurements were continuously taken of the film throughout the 6 h of illumination and the further 12 h of darkness.

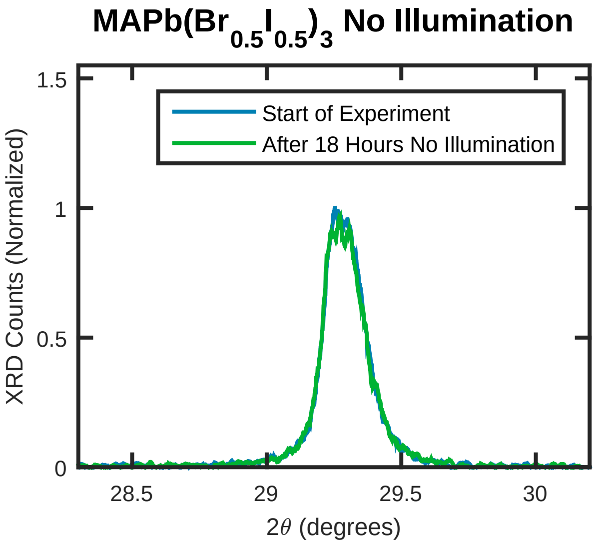

Figure S8: XRD patterns of an MAPb($Br_{0.5}I_{0.5}$)$_3$ thin film coated with PMMA, recorded before and after 18 h of darkness in the experimental setup. XRD measurements were continuously taken of the film throughout the 18 h of darkness.

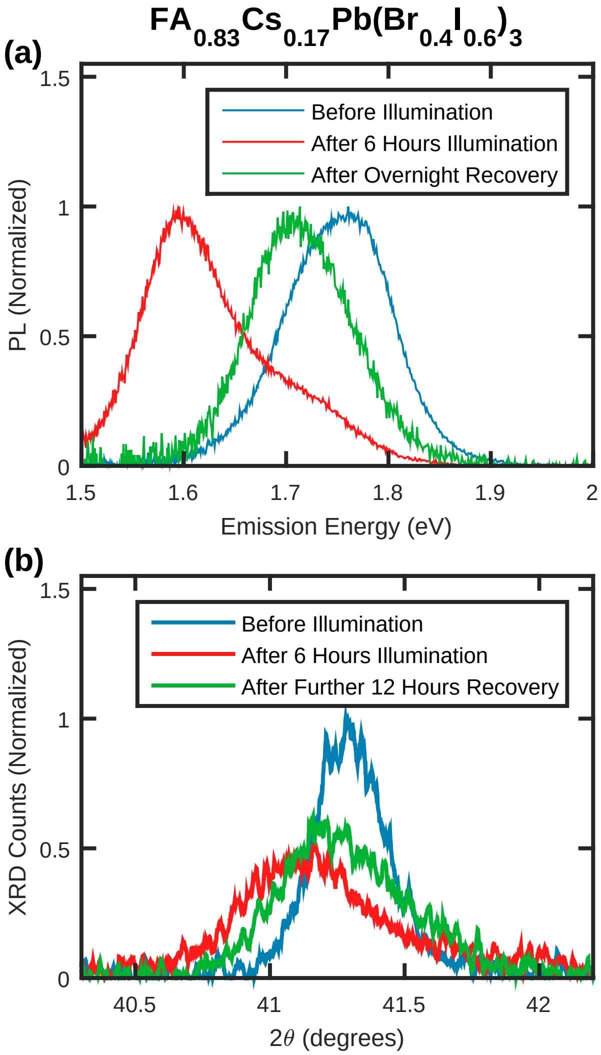

Figure S9: (a) PL spectra of an $FA_{0.83}Cs_{0.17}Pb(Br_{0.4}I_{0.6})_3$ thin film coated with PMMA, recorded before and after 6 h of 190 mW cm^{-2}, 470 nm wavelength illumination, and after a period of overnight recovery (around 18 h). (b) XRD patterns of the same film, recorded in-situ before and after the 6 h of 190 mW cm^{-2} illumination, and after a period of 12 h of darkness subsequent to the 6 h of illumination. “Before Illumination” (blue) data measurements in (a) and (b) were recorded at approximately the same time, as were the “After 6 Hours Illumination” (red) data measurements. XRD measurements were continuously taken of the film throughout the 6 h of illumination and the further 12 h of darkness.

5.4 Similar Behavior of Different Peaks

In order to evaluate whether the behavior observed in the (200) and (220) XRD peaks recorded from the MAPb($Br_{0.5}I_{0.5}$)$_3$ and $FA_{0.83}Cs_{0.17}$Pb($Br_{0.4}I_{0.6}$)$_3$ perovskite films is consistent across all peaks in the respective XRD patterns, Figures S10 and S11 present an XRD peak comparison for both an MAPb($Br_{0.5}I_{0.5}$)$_3$ (Figure S10) and $FA_{0.83}Cs_{0.17}$Pb($Br_{0.4}I_{0.6}$)$_3$ (Figure S11) thin film.

Figures S10a&b present the (100) and (200) XRD peaks, respectively, recorded from an MAPb($Br_{0.5}I_{0.5}$)$_3$ thin film, with the XRD measurements taken before the film was exposed to any illumination, and after the film was exposed to a 6 h period of $190\,\mathrm{mW\,cm^{-2}}$, 470 nm wavelength illumination followed by a period of overnight recovery (around 18 h). The XRD patterns in Figure S10 were obtained with a Rigaku Smartlab X-ray diffractometer, and were taken from diffraction angle 10° to 50° 2θ, at a scan speed of $0.02\,^{\circ}\,\mathrm{s^{-1}}$. The Cu-$K_{\alpha 1}$ line was used as incident radiation, and in order to correct against sample tilt, a relevant z-cut quartz peak in the data was used as a reference and fixed to 2θ=16.43°. The data shown in blue in Figure S10 is the same as that shown in green in Figure S1.

Figure S11a&b present the (220) and (221) XRD peaks, respectively, recorded from an $FA_{0.83}Cs_{0.17}$Pb($Br_{0.4}I_{0.6}$)$_3$ thin film, with the XRD measurements taken in-situ under 6 h of $190\,\mathrm{mW\,cm^{-2}}$, 470 nm wavelength illumination utilizing our experimental setup described in Section 5.1. The Cu-$K_{\alpha 1}$ line was used as incident radiation. Figure S11a shows identical data of the (220) peak to that shown in Figure 1d in the main text, but which are repeated here to allow for an easier comparison to the (221) peak data in Figure S11b to be made. The arrows indicate the behavior of the peaks over the 6 h of illumination.

The (100) and (200) peaks from the MAPb($Br_{0.5}I_{0.5}$)$_3$ thin film shown in Figures S10a&b, respectively, both display extremely similar decreases in amplitude and a high-angle tail-growth – or a shift to higher 2θ angles – as a result of the 6 h of illumination and subsequent overnight recovery. Figure S10 therefore suggests that the peak behaviors across the whole XRD pattern of the MAPb($Br_{0.5}I_{0.5}$)$_3$ sample were consistent over the course of the exper-

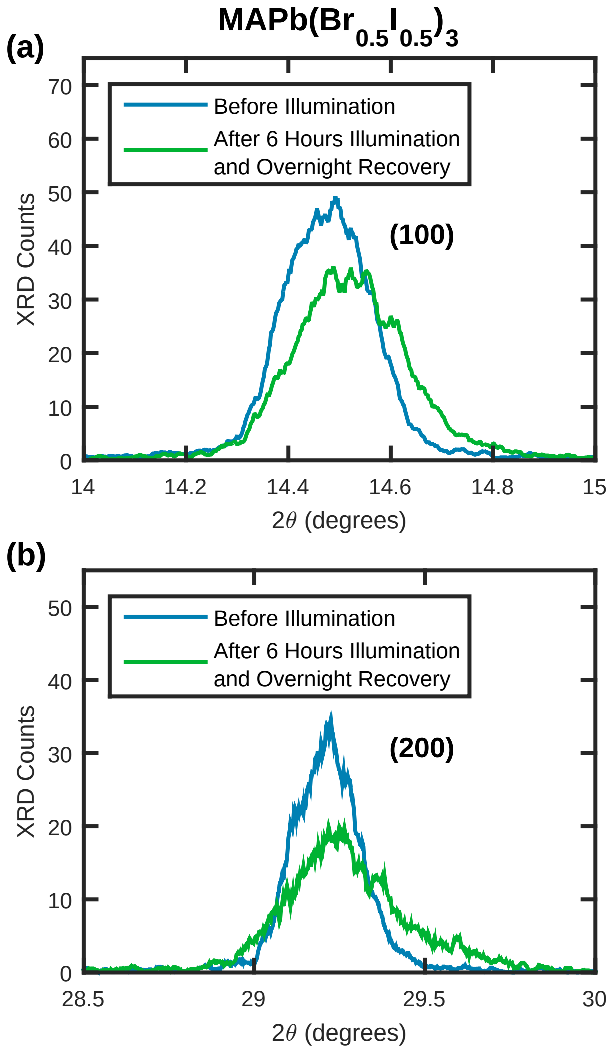

Figure S10: XRD patterns recorded from an $MAPb(Br_{0.5}I_{0.5})_3$ thin film coated with PMMA, recorded prior to any illumination, and after a 6 h period of 190 mW cm^{-2}, 470 nm wavelength illumination followed by a period of overnight recovery (around 18 h). Figures (a) and (b) are scaled to highlight the (100) and (200) peaks in the XRD patterns, respectively.

iment. The (220) and (221) peaks from the $FA_{0.83}Cs_{0.17}Pb(Br_{0.4}I_{0.6})_3$ thin film shown in Figures S11a&b, respectively, display near-identical decreases in amplitude, shifts to lower 2θ angles, and increases in peak widths over the course of the 6 h of illumination. Figure S11 therefore suggests that the peak behavior across the whole XRD pattern of the $FA_{0.83}Cs_{0.17}Pb(Br_{0.4}I_{0.6})_3$ sample was consistent over the course of the experiment.

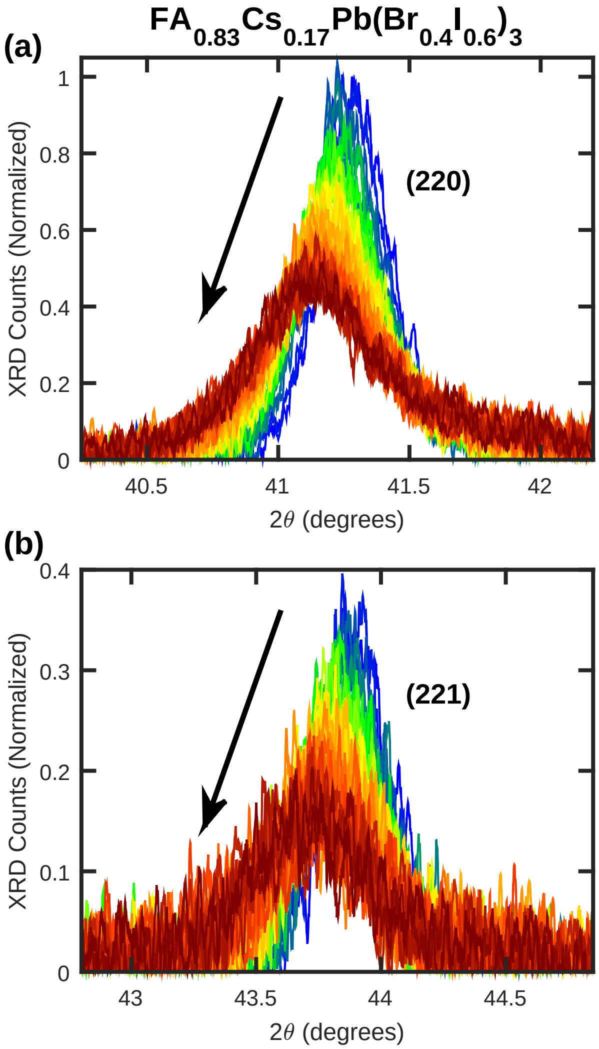

Figure S11: XRD patterns recorded from an $FA_{0.83}Cs_{0.17}Pb(Br_{0.4}I_{0.6})_3$ thin film coated with PMMA over the course of 6 h of 190 mW cm^{-2}, 470 nm wavelength illumination. Figures (a) and (b) are scaled to highlight the (220) and (221) peaks in the XRD patterns, respectively.

6 Lack of PbI_2 Accretion

Figure S12 and S13 display XRD patterns recorded from the $MAPb(Br_{0.5}I_{0.5})_3$ and $FA_{0.83}Cs_{0.17}Pb(Br_{0.4}I_{0.6})_3$ perovskite thin film samples, respectively, used in the experiments that are discussed in the main text. The data is plotted over the 2θ region where PbI_2 XRD peaks are most prominent. Figure S12a and S13a show zoomed regions of Figure S1 and S2, respectively, and Figure S12b and S13b were taken via the same experimental method as for Figure S12a and S13a, respectively, as detailed in Section 2.

Figure S12 shows that there was negligible XRD signal recorded from the $MAPb(Br_{0.5}I_{0.5})_3$ perovskite thin films that could be attributed to PbI_2, either before (Figure S12a) or after (Figure S12b) illumination. The peaks in the XRD patterns presented in Figure S13 are attributed to small amounts of PbI_2 in the measured $FA_{0.83}Cs_{0.17}Pb(Br_{0.4}I_{0.6})_3$ perovskite thin film sample. The lack of change in the PbI_2 XRD peak before (Figure S13a) and after (Figure S13b) the perovskite film was exposed to illumination shows that there was no degradation of perovskite material into PbI_2 during the conducted experiment discussed in the main text.

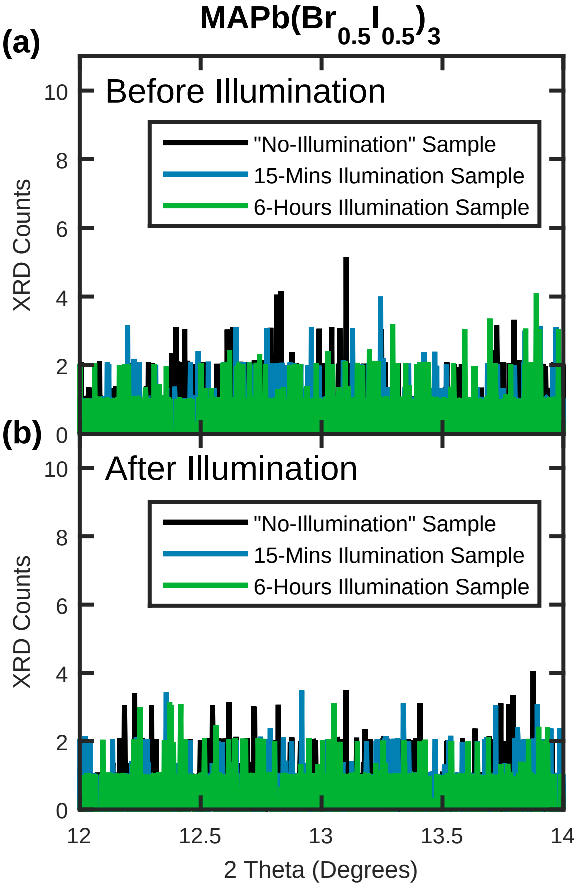

Figure S12: XRD patterns of three $MAPb(Br_{0.5}I_{0.5})_3$ thin films coated with PMMA, recorded (a) before and (b) after different lengths of illumination period (all at 190 mW cm^{-2} intensity and 470 nm wavelength) and a period of overnight recovery in the dark. The axes are scaled to show the region of the XRD pattern where peaks pertaining to any PbI_2 or $PbBr_2$ in the perovskite films would be visible. Given the lack of any significant signal in both (a) and (b), we conclude that there was no significant degradation of perovskite material into either PbI_2 or $PbBr_2$ during the conducted experiments.

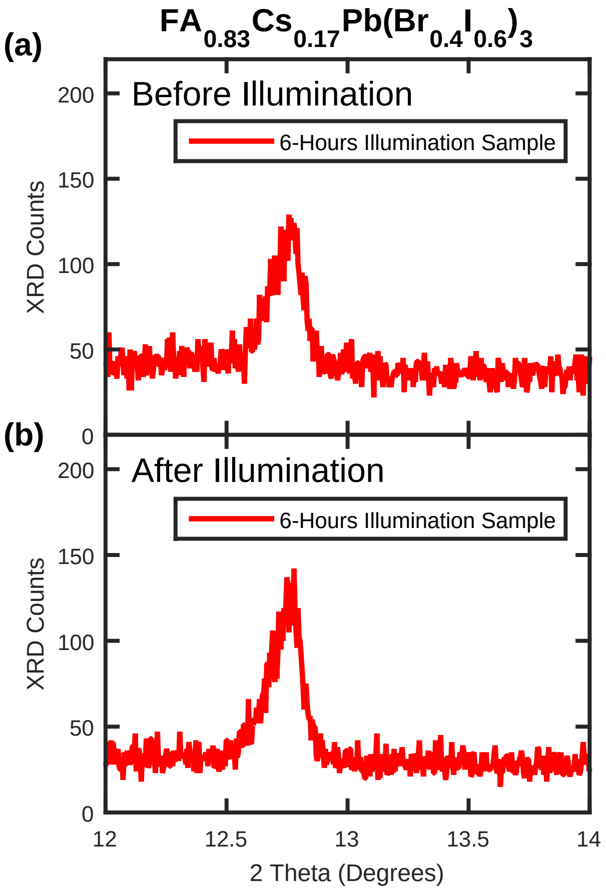

Figure S13: XRD patterns of an $FA_{0.83}Cs_{0.17}Pb(Br_{0.4}I_{0.6})_3$ thin film coated with PMMA, recorded (a) before and (b) after 6 h of illumination (at 190 mW cm^{-2} intensity and 470 nm wavelength) and a period of overnight recovery in the dark. The axes are scaled to show the region of the XRD pattern where peaks pertaining to any PbI_2 or $PbBr_2$ in the perovskite films would be visible. The visible signal in this region highlights that there were small amounts of PbI_2 or $PbBr_2$ in the perovskite film. However, given the near-identical signal between (a) and (b), we conclude that there was no significant degradation of perovskite material into either PbI_2 or $PbBr_2$ over the course of the conducted experiment.

7 Estimation of Perovskite Bromide Content

The PL emission energy of a mixed-halide perovskite material is influenced by its halide content.[S13,S17,S19] Similarly, the lattice spacings within a mixed-halide perovskite material – which influence the 2θ position of measured XRD peaks – are also dependant on the halide content of the perovskite.[S5,S11,S17,S19] Thus, assuming that the chemical composition of a given perovskite is determined by the ratio of the halide ions in the material, an estimate of the halide ratio in the perovskite can be made from measurements of either the emission energy or the 2θ position of a known XRD peak and the comparison of such data with those for perovskites with known compositions. In essence, one conversion formula needs to be determined that allows conversion of a PL emission energy into an estimate of the halide content of the emitting perovskite, and another for converting XRD peak position into an estimate of the halide content of the reflecting perovskite. By converting the horizontal axes (axes of abscissa) for both PL and XRD data such that they are provided in terms of an estimate of the halide content of the investigated mixed-halide perovskite, it is possible to draw comparisons between its optoelectronic and structural properties. This section details how these conversion formulae were created for use in our study.

From here on, we refer to ABX_3 perovskites for which B is lead, X is a mixture of iodide and bromide ions, and A is arbitrary but fixed: $APb(Br_xI_{(1-x)})_3$. This particular perovskite composition is most relevant for our work, although we note that the analysis presented in this section could be applied to other perovskites with different compositions.

7.1 Estimation Process Based on PL Measurements

In order to create a conversion formula between the PL emission energy of a mixed-halide perovskite and its bromide content, PL measurements must first be made of similar perovskites with known compositions. PL measurements of $APb(Br_xI_{(1-x)})_3$ perovskite films with known, differing bromide contents, x, allow for an estimate of the PL emission energy,

E, to be made across the bromide compositional range. Typically the PL peak emission energy is found to follow a quadratic behavior (referred to as band bowing) as a function of x:[S13,S17,S19]

$$E = ax^2 + bx + c \tag{1}$$

where a, b and c are parameters determined from the fit of x to the experimentally derived values of E.

Equation 1 can be inverted by finding the correct polynomial root, resulting in:

$$x = \frac{-b + \sqrt{b^2 - 4a(c - E)}}{2a} \tag{2}$$

Thus, the bromide content, x, of a perovskite can be directly related to PL photon emission energy, E, by inserting E into Equation 2, once a, b and c have been determined from measurements of known perovskite compositions. Therefore, Equation 2 was used as a conversion formula to convert the photon-emission-energy-axis of the PL spectra plot from emission energy, E, to bromide content, x, as detailed in the main article.

7.2 Estimation Process Based on XRD Measurements

In order to create a conversion formula between the 2θ position of a given XRD peak recorded from a perovskite and its bromide content, XRD measurements must first be made of similar perovskites with known compositions. XRD measurements of $\mathrm{APb(Br}_x\mathrm{I}_{(1-x)})_3$ perovskite films with known, differing bromide contents, x, allow for an estimate of the 2θ position of a given XRD peak to be made across the bromide compositional range. The 2θ position of an XRD peak is related to the distance between the lattice planes that coherently reflected the XRD signal through Bragg's Law:[S11]

$$2d \sin\theta = n\lambda \tag{3}$$

where d is the distance between the lattice planes that generate the XRD peak, n is a positive integer, and λ is the wavelength of the incident X-rays.

For a cubic crystal system, the distance between a given set of lattice planes, d, is related to the lattice spacing of the material, a, by the following relationship:[S11]

$$d = \frac{a}{\sqrt{h^2 + k^2 + l^2}} \tag{4}$$

Where h, k and l are the Miller indices of the given set of lattice planes. Via Equations 3 and 4, it is possible to calculate the lattice spacing, a, of a perovskite from the measured 2θ position of an XRD peak with known h, k and l. Accordingly, this calculation can be performed for a set of perovskites spanning a range of bromide ratios, x, to investigate the relation between bromide content and the resulting perovskite lattice spacing, a. Vegard's law – an empirical law – states that a linear relationship should be found between x and a, i.e. $a = \alpha x + \beta$. This relationship is usually observed in mixed-halide perovskites, and experimental measurements can determine the value of the fitting constants α and β.

Combining Equations 3 and 4 leads to the following equation for a:

$$a = \frac{\lambda\sqrt{h^2 + k^2 + l^2}}{2\sin\theta} \tag{5}$$

Where n has been folded into the Miller indices. Utilizing the linear fit between x and a allows for the derivation of the following equation:

$$x = \frac{\lambda\sqrt{h^2 + k^2 + l^2}}{2\alpha\sin\theta} - \frac{\beta}{\alpha} \tag{6}$$

Thus, the bromide content, x, of a perovskite can be estimated by measuring the 2θ position of an XRD peak with known h, k and l indices via an X-ray beam of known wavelength, λ, and inserting the appropriate values into Equation 6, given that α and β have been determined from measurements of known perovskite compositions. Therefore, Equation 6 was used as a conversion formula to convert the angle-axis of an XRD pattern plot from 2θ to bromide content, x, as described in the main article.

7.3 Estimates for $\mathrm{MAPb(Br_{0.5}I_{0.5})_3}$

In order to estimate the bromide content of perovskite regions within $\mathrm{MAPb(Br_{0.5}I_{0.5})_3}$ thin films from recorded PL data, calculations were performed as according to Section 7.1 above. PL spectra reported in the literature were used to determine the relationship between bromide content, x, and $\mathrm{MAPb(Br_xI_{(1-x)})_3}$ PL emission energy, specifically from Ref. S13, S17, and S19.

In order to estimate the bromide content of perovskite regions within $\mathrm{MAPb(Br_{0.5}I_{0.5})_3}$ thin films from recorded XRD data, calculations were performed as according to Section 7.2 above. XRD patterns reported in the literature were used to determine the relationship between bromide content, x, and the 2θ value of the (200) peak of $\mathrm{MAPb(Br_xI_{(1-x)})_3}$ perovskites, specifically from Ref. S17 and S19. A slight complication arose in the analysis from the phase transition of $\mathrm{MAPb(Br_xI_{(1-x)})_3}$ perovskites around $x = 0.2$, however this was overcome by performing the relevant calculations for both phases of the perovskite.

7.4 Estimates for $\mathrm{FA_{0.83}Cs_{0.17}Pb(Br_{0.4}I_{0.6})_3}$

In order to estimate the bromide content of perovskite regions within $\mathrm{FA_{0.83}Cs_{0.17}Pb(Br_{0.4}I_{0.6})_3}$ thin films from recorded PL data, calculations were performed as according to Section 7.1 above. PL results for $\mathrm{FA_{0.83}Cs_{0.17}Pb(Br_xI_{(1-x)})_3}$ perovskites across the entire $x = 0$ to $x = 1$ compositional range (steps of $x = 0.1$) were recorded in-house, as shown in Figure S14. PL spectra were recorded by illuminating the thin film samples with light from a 405 nm laser at an intensity of $\sim 100\,\mathrm{mW\,cm^{-2}}$ when placed in an integrating sphere. The PL spectra were recorded using a QEPRO-FL spectrometer.

In order to estimate the bromide content of perovskite regions within our $\mathrm{FA_{0.83}Cs_{0.17}Pb(Br_{0.4}I_{0.6})_3}$ thin films from recorded XRD data, calculations were performed

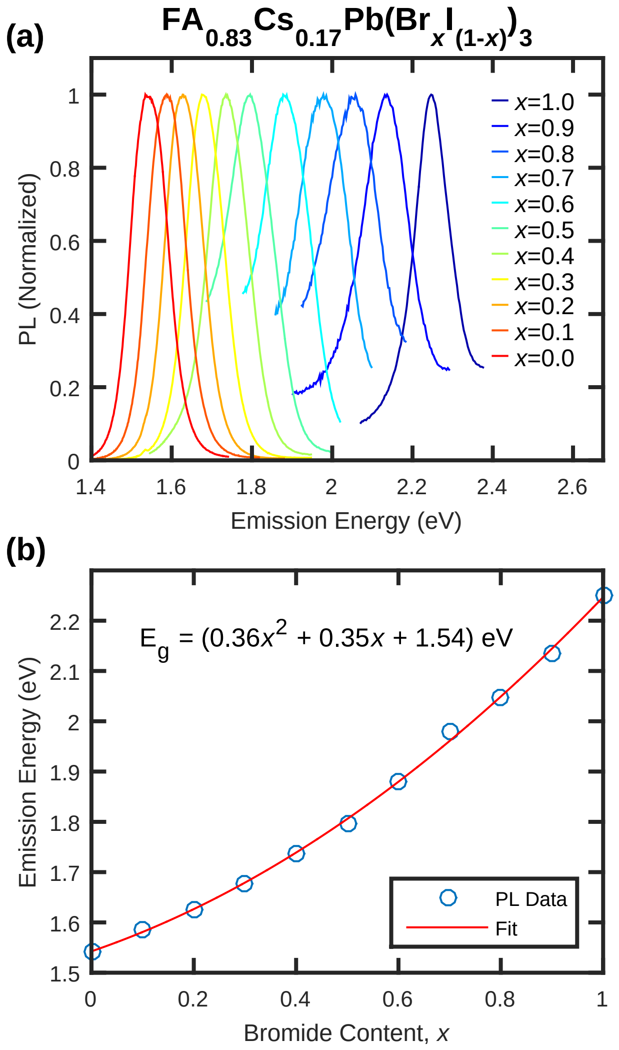

Figure S14: (a) PL spectra showing the high energy, mixed perovskite PL peak from $FA_{0.83}Cs_{0.17}Pb(Br_xI_{(1-x)})_3$ thin films ranging in composition from $x = 1.0$ to $x = 0.0$. The illumination source was at $100\,mW\,cm^{-2}$ intensity and 405 nm wavelength. (b) The centre emission energy of the PL peaks shown in (a) plotted against the bromide content of the perovskite, x. Fitted to this data is a quadratic curve, which is used as a conversion between PL emission energy and estimated bromide content in Figure 4a of the main text. The PL emission energy exhibits a mild bowing across the compositional range, similar to that previously observed for this perovskite composition.[S5]

as according to Section 7.2 above. XRD patterns reported in the literature were used to determine the relationship between bromide content, x, and the 2θ value of the (220) peak of $FA_{0.83}Cs_{0.17}Pb(Br_xI_{(1-x)})_3$ perovskites, specifically from Ref. S5.

8 $MAPb(Br_{0.5}I_{0.5})_3$ Crystallite Size Estimation

The fracturing of a crystalline material into smaller crystalline domains results in the broadening of the recorded XRD peaks from the material.[S20] As a result, the size of the crystalline domains within the measured material can be estimated from the width of the recorded XRD peaks according to the Scherrer equation:[S20]

$$D = \frac{K\lambda}{\beta \cos\theta} \tag{7}$$

Where D is the size estimate of the crystalline domains, K is a dimensionless shape factor that is assumed to be equal to 1 for the purposes of the crystalline size estimates presented here, λ is the wavelength of the incident X-rays used for the XRD measurement, β is the full width at half maximum (FWHM) of the investigated XRD peak when measured in radians, and θ is the Bragg angle of the investigated peak. Equation 7 allows an estimate of the crystalline domain size within a sample to be made from measurements of a corresponding XRD peak. We note that this XRD peak analysis is only perfectly valid if the material is compositionally homogeneous, which is not expected to be true for materials experiencing halide segregation, and for such materials this analysis is expected to only give an estimate of the lower bound to the crystalline domain size of the material. In addition, other factors not accounted for by our use of Equation 7 – such as the true from of K – may introduce further errors into the analysis presented in this section, which we emphasize is only meant to highlight the relationship between XRD peak broadening and crystallite size breakdown, rather than to provide accurate estimates of the crystalline domain sizes within our perovskite films.

Figure S15a presents the FWHM of the (200) peak from XRD patterns recorded from an $MAPb(Br_{0.5}I_{0.5})_3$ perovskite thin film over 6 h of illumination at $190\,\mathrm{mW\,cm^{-2}}$ intensity and 470 nm wavelength – see Figure S7 for XRD patterns and PL spectra recorded from this $MAPb(Br_{0.5}I_{0.5})_3$ film. The FWHM was estimated both directly from the data, and

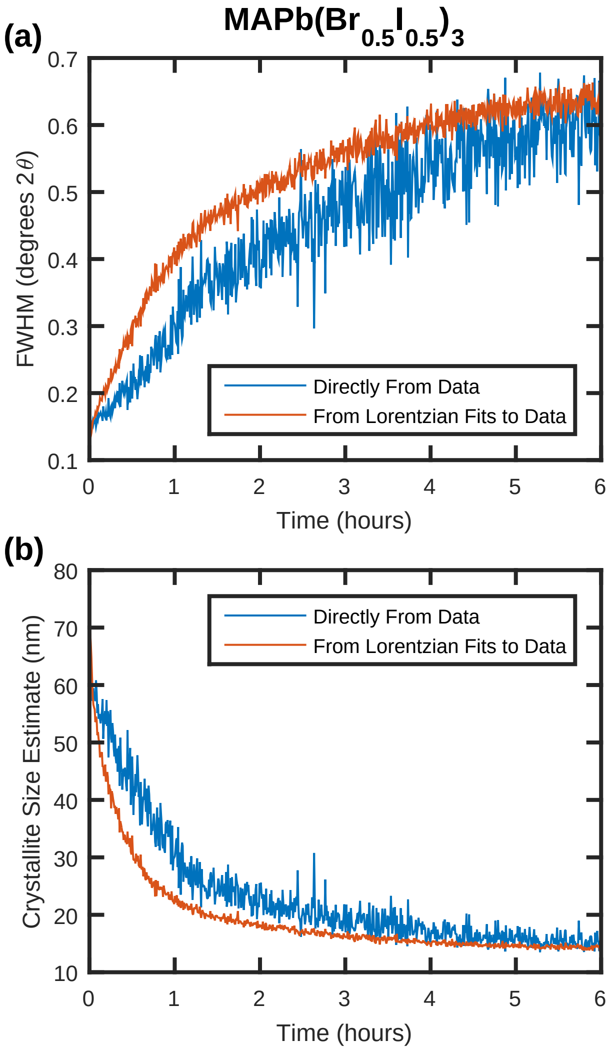

Figure S15: (a) The full width at half maximum (FWHM) of the (200) peak in XRD patterns recorded from an MAPb($Br_{0.5}I_{0.5}$)$_3$ perovskite thin film over 6 h of illumination at 190 mW cm^{-2} intensity and 470 nm wavelength. Plotted in blue is the FWHM estimated directly from the data, and in orange is the FWHM taken from Lorentzian fits to the XRD data. (b) Mean size of the crystalline domains within the MAPb($Br_{0.5}I_{0.5}$)$_3$ perovskite thin film, estimated using the Scherrer equation[S20] – Equation 7 – and the XRD peak widths shown in (a). We note that due to other effects such as compositional inhomogeneities, the crystallite size estimates presented in (b) should only be considered as estimates to the lower bound of the crystalline domain sizes within the MAPb($Br_{0.5}I_{0.5}$)$_3$ film.

from Lorentzian fits to the data. Figure S15b presents estimates of the crystalline domain size within the MAPb($Br_{0.5}I_{0.5}$)$_3$ film over the course of the 6 h of illumination, calculated using Equation 7, and the FWHM estimates shown in Figure S15a. A clear widening of the (200) XRD peak over the course of the experiment is shown in Figure S15a, and Figure

S15b shows that the crystallite size estimate correspondingly decreases during the period of illumination. As mentioned in the main text, the widening of the XRD peak as shown in Figure S15a is likely also partly the result of ionic redistribution throughout the material, and so the crystallite size estimates presented in Figure S15b should only be considered as estimates of the lower bound of the crystalline domain sizes within the $MAPb(Br_{0.5}I_{0.5})_3$ film.

References

(S1) Noel, N. K.; Habisreutinger, S. N.; Wenger, B.; Klug, M. T.; Hörantner, M. T.; Johnston, M. B.; Nicholas, R. J.; Moore, D. T.; Snaith, H. J. A Low Viscosity, Low Boiling Point, Clean Solvent System for the Rapid Crystallisation of Highly Specular Perovskite Films. *Energy Environ. Sci.* **2017**, *10*, 145–152.

(S2) Lin, Y.-H.; Sakai, N.; Da, P.; Wu, J.; Sansom, H. C.; Ramadan, A. J.; Mahesh, S.; Liu, J.; Oliver, R. D. J.; Lim, J. et al. A Piperidinium Salt Stabilizes Efficient Metal-Halide Perovskite Solar Cells. *Science* **2020**, *369*, 96–102.

(S3) Rehman, W.; McMeekin, D. P.; Patel, J. B.; Milot, R. L.; Johnston, M. B.; Snaith, H. J.; Herz, L. M. Photovoltaic Mixed-Cation Lead Mixed-Halide Perovskites: Links Between Crystallinity, Photo-Stability and Electronic Properties. *Energy Environ. Sci.* **2017**, *10*, 361–369.

(S4) Braly, I. L.; Stoddard, R. J.; Rajagopal, A.; Uhl, A. R.; Katahara, J. K.; Jen, A. K.-Y.; Hillhouse, H. W. Current-Induced Phase Segregation in Mixed Halide Hybrid Perovskites and its Impact on Two-Terminal Tandem Solar Cell Design. *ACS Energy Lett.* **2017**, *2*, 1841–1847.

(S5) McMeekin, D. P.; Sadoughi, G.; Rehman, W.; Eperon, G. E.; Saliba, M.; Hörantner, M. T.; Haghighirad, A.; Sakai, N.; Korte, L.; Rech, B. et al. A Mixed-Cation Lead Mixed-Halide Perovskite Absorber for Tandem Solar Cells. *Science* **2016**, *351*, 151–155.

(S6) Knight, A.; Herz, L. M. Preventing Phase Segregation in Mixed-Halide Perovskites: A Perspective. *Energy Environ. Sci.* **2020**, *13*, 2024–2046.

(S7) Nandi, P.; Giri, C.; Swain, D.; Manju, U.; Mahanti, S. D.; Topwal, D. Temperature Dependent Photoinduced Reversible Phase Separation in Mixed-Halide Perovskite. *ACS Appl. Energy Mater.* **2018**, *1*, 3807–3814.

(S8) Noel, N. K.; Wenger, B.; Habisreutinger, S. N.; Patel, J. B.; Crothers, T.; Wang, Z.; Nicholas, R. J.; Johnston, M. B.; Herz, L. M.; Snaith, H. J. Highly Crystalline Methylammonium Lead Tribromide Perovskite Films for Efficient Photovoltaic Devices. *ACS Energy Lett.* **2018**, *3*, 1233–1240.

(S9) Rothmann, M. U.; Kim, J. S.; Borchert, J.; Lohmann, K. B.; O'Leary, C. M.; Sheader, A. A.; Clark, L.; Snaith, H. J.; Johnston, M. B.; Nellist, P. D. et al. Atomic-Scale Microstructure of Metal Halide Perovskite. *Science* **2020**, *370*.

(S10) Harbeke, G.; Tosatti, E. Band-Edge Excitons in PbI_2: A Puzzle? *Phys. Rev. Lett.* **1972**, *28*, 1567.

(S11) Simon, S. H. *The Oxford Solid State Basics*; OUP Oxford, 2013.

(S12) Slimi, B.; Mollar, M.; Assaker, I. B.; Kriaa, A.; Chtourou, R.; Marí, B. Synthesis and Characterization of Perovskite $FAPbBr_{3-x}I_x$ Thin Films for Solar Cells. *Monatsh. Chem.* **2017**, *148*, 835–844.

(S13) Jacobsson, T. J.; Correa-Baena, J.-P.; Pazoki, M.; Saliba, M.; Schenk, K.; Grätzel, M.; Hagfeldt, A. Exploration of the Compositional Space for Mixed Lead Halogen Perovskites for High Efficiency Solar Cells. *Energy Environ. Sci.* **2016**, *9*, 1706–1724.

(S14) Beal, R. E.; Slotcavage, D. J.; Leijtens, T.; Bowring, A. R.; Belisle, R. A.; Nguyen, W. H.; Burkhard, G. F.; Hoke, E. T.; McGehee, M. D. Cesium Lead Halide Perovskites with Improved Stability for Tandem Solar Cells. *J. Phys. Chem. Lett.* **2016**, *7*, 746–751.

(S15) Yoon, S. J.; Stamplecoskie, K. G.; Kamat, P. V. How Lead Halide Complex Chemistry Dictates the Composition of Mixed Halide Perovskites. *J. Phys. Chem. Lett.* **2016**, *7*, 1368–1373.

(S16) Xie, Y.-M.; Zeng, Z.; Xu, X.; Ma, C.; Ma, Y.; Li, M.; Lee, C.-S.; Tsang, S.-W. FA-Assistant Iodide Coordination in Organic–Inorganic Wide-Bandgap Perovskite with Mixed Halides. *Small* **2020**, *16*, 1907226.

(S17) Hoke, E. T.; Slotcavage, D. J.; Dohner, E. R.; Bowring, A. R.; Karunadasa, H. I.; McGehee, M. D. Reversible Photo-Induced Trap Formation in Mixed-Halide Hybrid Perovskites for Photovoltaics. *Chem. Sci.* **2015**, *6*, 613–617.

(S18) Rehman, W.; Milot, R. L.; Eperon, G. E.; Wehrenfennig, C.; Boland, J. L.; Snaith, H. J.; Johnston, M. B.; Herz, L. M. Charge-Carrier Dynamics and Mobilities in Formamidinium Lead Mixed-Halide Perovskites. *Adv. Mater.* **2015**, *27*, 7938–7944.

(S19) Noh, J. H.; Im, S. H.; Heo, J. H.; Mandal, T. N.; Seok, S. I. Chemical Management for Colorful, Efficient, and Stable Inorganic–Organic Hybrid Nanostructured Solar Cells. *Nano Lett.* **2013**, *13*, 1764–1769.

(S20) Scherrer, P. Nachrichten von der Gesellschaft der Wissenschaften zu Göttingen. *Mathematisch-Physikalische Klasse* **1918**, *2*, 98–100.